



Published in final edited form as:

Neuroimage. 2022 September ; 258: 119399. doi:10.1016/j.neuroimage.2022.119399.

Detection of functional activity in brain white matter using fiber architecture informed synchrony mapping

Yu Zhao^{a,b,*}, Yurui Gao^{a,c}, Zhongliang Zu^{a,b}, Muwei Li^{a,b}, Kurt G. Schilling^{a,c}, Adam W. Anderson^{a,b,c}, Zhaohua Ding^{a,c,f,*}, John C. Gore^{a,b,c,d,e}

^aVanderbilt University Institute of Imaging Science, United States

^bDepartment of Radiology and Radiological Sciences, Vanderbilt University Medical Center, United States

^cDepartment of Biomedical Engineering, Vanderbilt University, United States

^dDepartment of Molecular Physiology and Biophysics, Vanderbilt University, United States

^eDepartment of Physics and Astronomy, Vanderbilt University, United States

^fDepartment of Electrical and Computer Engineering, Vanderbilt University, United States

Abstract

A general linear model is widely used for analyzing fMRI data, in which the blood oxygenation-level dependent (BOLD) signals in gray matter (GM) evoked in response to neural stimulation are modeled by convolving the time course of the expected neural activity with a canonical hemodynamic response function (HRF) obtained a priori. The maps of brain activity produced reflect the magnitude of local BOLD responses. However, detecting BOLD signals in white matter (WM) is more challenging as the BOLD signals are weaker and the HRF is different, and may vary more across the brain. Here we propose a model-free approach to detect changes in BOLD signals in WM by measuring task-evoked increases of BOLD signal synchrony in WM fibers. The proposed approach relies on a simple assumption that, in response to a functional task, BOLD signals in relevant fibers are modulated by stimulus-evoked neural activity and thereby show greater synchrony than when measured in a resting state, even if their magnitudes do not change substantially. This approach is implemented in two technical stages. First, for each voxel a fiber-architecture-informed spatial window is created with orientation distribution functions

This is an open access article under the CC BY-NC-ND license (<http://creativecommons.org/licenses/by-nc-nd/4.0/>)

*Corresponding authors. yu.zhao.1@vumc.org (Y. Zhao), zhaohua.ding@vanderbilt.edu (Z. Ding).

Declaration of Competing Interest

The authors declare that they have no competing interests.

Credit authorship contribution statement

Yu Zhao: Conceptualization, Methodology, Software, Data curation, Formal analysis, Writing – original draft, Writing – review & editing. **Yurui Gao:** Data curation, Software, Writing – review & editing. **Zhongliang Zu:** Software. **Muwei Li:** Software. **Kurt G. Schilling:** Software. **Adam W. Anderson:** Supervision. **Zhaohua Ding:** Methodology, Writing – original draft, Writing – review & editing, Supervision. **John C. Gore:** Methodology, Writing – original draft, Writing – review & editing, Supervision.

Code and data availability

An implementation of the methods proposed in this work will be made available as a MATLAB package on GitHub at https://github.com/YuZhaoMRI/FAIW_PCA. Human MRI datasets used in this study were sourced from the WU-Minn Human Connectome Project (HCP) database.

constructed from diffusion imaging data. This provides the basis for defining neighborhoods in WM that share similar local fiber architectures. Second, a modified principal component analysis (PCA) is used to estimate the synchrony of BOLD signals in each spatial window. The proposed approach is validated using a 3T fMRI dataset from the Human Connectome Project (HCP) at a group level. The results demonstrate that neural activity can be reliably detected as increases in fMRI signal synchrony within WM fibers that are engaged in a task with high sensitivities and reproducibility.

Keywords

Functional MRI; White matter; Activation mapping; Graph signal processing; Synchrony mapping

1. Introduction

Functional MRI (fMRI) based on blood oxygenation level-dependent (BOLD) signals is well established for detecting and mapping neural activities in brain gray matter (GM). However, there are relatively few corresponding reports of fMRI studies of white matter (WM), partly due to continuing uncertainties regarding the sources of BOLD signals therein (Gawryluk et al., 2014; Mazerolle et al., 2020) as well as technical challenges in their reliable detection. Nonetheless, the existence and potential functional relevance of BOLD signals in WM have been validated by a growing number of recent studies, (see reviews in (Gore et al., 2019; Grajauskas et al., 2019)). These have been partially motivated by the fact that WM comprises about half of the brain parenchyma and plays an important role as the communication system of the brain, and so the functional properties of WM should be included in any complete model of brain organization. In addition, recent studies of diffusion fMRI demonstrate that neural activities in WM could trigger microstructural changes of axons, which provides a new perspective for functional studies of WM (Lin et al., 2014; Spees et al., 2013; Spees et al., 2018; Olszowy et al., 2021). In the emerging field of WM fMRI, analysis methods established for GM have been adopted and applied, including measures of function connectivity (Ding et al., 2018; Gao et al., 2021; Jiang et al., 2019) and spectral analysis (Huang et al., 2018; Marussich et al., 2017; Ji et al., 2019; Li et al., 2021), and these have shown the potential of characterizing selected features of WM in neurodegenerative and other disorders.

The standard approach that has been widely used in fMRI studies of GM uses a general linear model (GLM) to detect activations that correspond to a change in the local BOLD signal magnitude, but this may not be appropriate for WM as suggested by previous reports (Li et al., 2019). The GLM assumes that the BOLD response to stimulation may be treated as a linear shift-invariant system so that the BOLD signals can be modeled by convolving the time course of neural activities with a hemodynamic response function (HRF). The GLM assumes that evoked neural activations are synchronous with the timings of presented stimuli or tasks that trigger hemodynamic responses (Poline and Brett, 2012) and correspond to a change in signal magnitude. This assumption may not be valid in all situations, especially in WM because it ignores intrinsic brain activities that preexist in the background and are unrelated to extrinsic stimuli. Such intrinsic brain activities were

considered noise before they were found to predict spatial patterns of functional connectivity (i.e., functional networks) in a resting state (Zhang and Raichle, 2010; Laird et al., 2011). A voxel in WM contains a large number of axons that connect neurons in different positions in GM (Schilling et al., 2018; Voigt et al., 2019) and these may produce asynchronous neuronal signals so that fMRI signals measured in a WM voxel may be more complex than those in GM and thus inconsistent with stimuli in tasks. A further assumption in the GLM is that the HRF keeps fixed for all positions, as implemented in SPM (Poline and Brett, 2012). This assumption is not valid in all WM as previous studies have shown that HRFs measured in WM exhibit substantial regional variations (Li et al., 2019; Courtemanche et al., 2018). A potential solution to the issue of the spatially varying HRF is to use variants of a GLM that allow spatial-adaptive HRFs to be estimated by a set of Finite Impulse Response (FIR) bases (Kay et al., 2008). However, multiple coefficients associated with the set of FIR functional bases need to be determined in the modeling of HRF, where the noise-dependent overfitting in such approaches may prevent accurate activation mapping (Vincent et al., 2010). Moreover, many studies demonstrate that the hemodynamic responses characterized by BOLD signals are nonlinear in GM, where the hemodynamic responses are time-dependent and thus BOLD signals cannot be modeled by the convolution that is implemented in GLM (see the review in (Polimeni and Lewis, 2021)). The nonlinearity of hemodynamic responses would also exist in WM, which could also result in the invalidity of the GLM assumption. Besides, fMRI signal fluctuations in WM are substantially lower than those in GM (Yarkoni et al., 2009) due to the substantially lower blood volume in WM compared to GM (Gawryluk et al., 2014; Jochimsen et al., 2010) and the resulting lower BOLD signal-to-noise-ratio poses additional challenges to the analysis of WM.

A model-free approach, without the assumptions mentioned above, that produces robust detection of activity-related BOLD signals in WM is thus needed. An alternative to the GLM that incorporates the temporal coherence of a voxel with respect to its neighbors may provide a means of activation mapping without modeling the BOLD signal or assuming local changes in signal magnitude. This approach is inspired by previous findings that the regional homogeneity (ReHo) of fMRI signals in GM is modulated by stimuli presented in tasks (Zang et al., 2004; Yuan et al., 2013; Lv et al., 2013). The ReHo approach relies on the fact that voxels within a GM volume at a macroscopic scale constitute a functional unit in which the synchrony of inter-voxel time courses can be enhanced under functional loading. In contrast to GM, anatomical structures of the WM feature complex interwoven networks, in which fibrous tissues constitute elongated functional units for neural signal transmission and thus show structural anisotropy. Brain functional processes embedded in such an anisotropic substrate should also exhibit anisotropic spatial profiles. This has been demonstrated by previous studies of BOLD signals in WM (Ding et al., 2013; Ding et al., 2016; Schilling et al., 2019), which reported structure-specific temporal correlations along WM tracts in a resting state that become more pronounced in relevant structures under a task loading. Given the relationships between local fiber architectures and WM function, we propose a new approach for mapping activity-related BOLD signals in WM that incorporates a metric of BOLD signal synchrony. This approach introduces two technical innovations. First, an adaptive spatial window in the form of fiber-architecture informed neighborhood is created for each voxel, within which time courses are collected

and weighted. The neighborhood is determined using diffusion orientation distribution functions (ODFs) obtained from high angular resolution diffusion imaging (HARDI) data. A similar concept was proposed in a previous report that used anisotropic spatial filtering to enhance noisy BOLD contrasts in WM (Abramian et al., 2021). Second, a modified principal component analysis (PCA) is applied to time courses of fMRI data to estimate the synchrony of time courses within the fiberarchitecture-informed window of each voxel. Taken together, the proposed approach overcomes the intrinsic limitations of GLM based analyses of BOLD signals in WM.

In the following, the proposed model-free mapping of neural activations is illustrated using a 3T fMRI dataset from the Human Connectome Project (HCP) at a group level. First, spatial patterns within activation maps are evaluated by reference to anatomical structures of WM fibers derived from diffusion MRI. Then, the influence of task loading on activation are investigated by comparing activation maps derived from motor-task fMRI data with those acquired in a resting-state. Motor-task enhanced activations in WM are demonstrated in WM regions related to the primary motor cortex, or M1, which are determined by WM fiber tracking with seed points in M1. Furthermore, the sensitivity, specificity and reproducibility of the proposed method are assessed statistically based on fiber-tracking-based parcellations of task-related and unrelated WM regions.

2. Methods

The proposed approach consists of two major steps implemented on a voxel-by-voxel basis (Fig. 1). First, a fiber-architecture-informed spatial window is created for each voxel using ODFs constructed from HARDI data. Second, a modified PCA is used to estimate the synchrony of fMRI time courses based on this spatial window. Detailed algorithms and procedures of the proposed approach are described as follows.

2.1. Design of fiber-architecture-informed spatial window

Principles from the recently emerging field of graph signal processing (GSP) (Shuman et al., 2013; Ortega et al., 2018) provide an elegant framework to design the fiber-architecture-informed spatial window. Based on the GSP framework, we analyze fMRI time courses at a discrete set of positions, which form a set of vertices of a topological graph, in such a way that underlying constraints from fiber architectures can be accounted for by edges of the graph. Here, we denote a graph as $\mathbf{G} = \{\mathbf{V}, \mathbf{E}, \mathbf{W}$ as usual, which consists of a finite set of vertices \mathbf{V} with $|\mathbf{V}| = N$, a set of edges \mathbf{E} , and a weighted connection matrix \mathbf{W} . $W_{i,j}$ represents the connection strength of edge $e = (i, j)$ that connects vertices i and j . On the vertices of the graph, we define a vector $\mathbf{f} \in \mathbb{R}^N$ to represent a set of auxiliary quantities to be used to generate spatial windows, where the i -th component of the vector, $\mathbf{f}(i)$, represents the value at the i -th vertex in \mathbf{V} .

For this study, voxel-wise graphs are constructed using ODFs derived from HARDI data with an isotropic voxel size, which have been well described in previous reports (Abramian et al., 2021; Iturria-Medina et al., 2007). In each graph, every vertex corresponds to a voxel in 3D MR images with weighted connections to its neighbors. The connection weight of any two neighboring voxels depends on the coherence of diffusion orientations between

the two voxels. As a result, two neighboring voxels residing in the same fiber tract have relative larger weight than those in different fiber tracts. Note that a high angular resolution, a high voxel resolution and an isotropic voxel size of diffusion MRI data are beneficial to accurately characterize fiber-architecture-informed connections in the graph.

Building on the topological properties of the fiber-architecture-informed graph, a spatial window is created for each vertex/voxel by simulating diffusion on the graph with point sources located at each vertex. A kernel is defined for the diffusion process in the spectral domain, which is derived from a Laplacian matrix defined in GSP. Specifically, a Laplacian matrix of \mathbf{G} is defined as $\mathbf{L} = \mathbf{D} - \mathbf{W}$, where \mathbf{D} denotes the graph's degree matrix, which is diagonal with elements $d_{i,i} = \sum_j w_{i,j}$; the graph operator \mathbf{L} is a real symmetric matrix, and thus has a complete set of orthonormal eigenvectors $\{u_\ell\}_{\ell=1,2,\dots,N}$ and associated eigenvalues $\{\lambda_\ell\}_{\ell=1,2,\dots,N}$ satisfying $\mathbf{L}u_\ell = \lambda_\ell u_\ell$. With these eigenvectors, the graph signal \mathbf{f} can be transformed into the spectral domain,

$$\hat{\mathbf{f}}(\ell) = \sum_{i=1}^N u_\ell^T(i) \mathbf{f}(i) = u_\ell^T \mathbf{f}, \ell = 1, 2, \dots, N \quad (1)$$

This spectral representation allows an exact reconstruction, i.e., the signal \mathbf{f} can be recovered as

$$\mathbf{f} = \sum_{\ell=1}^N \hat{\mathbf{f}}(\ell) u_\ell. \quad (2)$$

In the graph spectral domain, the kernel of diffusion (Turner, 2002) can be defined as

$$K(\lambda) = e^{-\tau\lambda} \quad (3)$$

where τ is a free parameter determining the spatial extent of diffusion on a graph, and it can be intuitively treated as the duration of diffusion. Given an initial point source \mathbf{f}_0 ($t=0$), the transient diffusion profile at time point t can be derived as

$$\mathbf{f}(t) = \sum_{\ell=1}^N K(\lambda_\ell) \hat{\mathbf{f}}_0(\ell) u_\ell = \sum_{\ell=1}^N e^{-\lambda_\ell t} u_\ell^T \mathbf{f}_0 u_\ell \quad (4)$$

To create a spatial window centered at a voxel i we define this point source by setting the initial profile \mathbf{f}_0 to be equal to 1 at the position i and 0 otherwise. The transient profile $\mathbf{f}(t)$ at the time point t is further processed to yield the fiber-architecture-informed spatial window, the width of which can be adjusted by the parameter τ . To be specific, the window is defined by taking voxels with M largest values of $\mathbf{f}(t)$, which is subsequently normalized with their summation,

$$\mathbf{F}_i(j) = \mathbf{f}(j, \tau) / \sum_{j=1}^M \mathbf{f}(j, \tau) \quad (5)$$

In this study, the largest parameter M is taken under an empirical constraint $\sum_{j=1}^M \mathbf{f}(j, \tau) > 0.95$, wherein small values in the diffusion profile of each voxel are removed to improve computational efficiency.

2.2. PCA based on fiber-architecture-informed window

In previous reports, the synchrony of fMRI time-courses in a parcellated region have been quantified using PCA (Tian et al., 2020), wherein the variance explained by the first principal component gauges the extent of synchrony. Here, the conventional PCA is modified to allow the integration of fiber architecture information, referred to as a modified PCA based on a fiber-architecture-informed window (FAIW-PCA). Basically, the raw fMRI time courses are first normalized with respect to the mean values and the standard deviations. Then, within each window F_i centered at the position i , the normalized time courses are rearranged into a matrix (X) of dimension $T \times M$, where T denotes the number of time frames and M the number of voxels within the window. We denote a time course in X as x_j , the i -th column in the matrix X , and formulate the FAIW-PCA as an optimization problem, where the first principal component v_1 can be obtained by

$$v_1 = \arg \max_{\|v\|=1} \left\{ \sum_{j=1}^M \mathbf{F}_i(j) \cdot (x_j \cdot v)^2 \right\} \quad (6)$$

Note that, without the weights $\mathbf{F}_i(j)$, this optimization problem will degenerate into a conventional PCA. Here, $\mathbf{F}_i(j)$ is applied in the optimization such that the time courses associated with the voxels near the center position are emphasized more in the first principal component obtained, which emphasizes the spatial specificity of the synchrony estimate. We further write this optimization in matrix form,

$$v_1 = \arg \max_{\|v\|=1} \left\{ v^T X^T Q X v \right\} \quad (7)$$

where the matrix $Q = \text{diag} [\mathbf{F}_i(1), \mathbf{F}_i(2), \dots, \mathbf{F}_i(M)]$. With simple algebraic manipulations, Eq. (7) can be written as

$$v_1 = \arg \max \left\{ \frac{v^T H v}{v^T v} \right\} \quad (8)$$

where $H = X^T Q X$. H is a positive-definite matrix, and thus has a complete set of orthonormal eigenvectors $\{v_\ell, \ell=1, 2, \dots, M\}$ and associated eigenvalues $\{\sigma_\ell, \ell=1, 2, \dots, M\}$, $\sigma_\ell \geq \sigma_{\ell+1} \geq 0$ that satisfy $H v_\ell = \sigma_\ell v_\ell$. The quantity to be maximized in Eq. (8) is a Rayleigh quotient. The quotient's maximum possible value is the largest eigenvalue σ_1 , which is associated with the solution v_1 . Finally, the synchrony of time courses is estimated by

$$\text{Synchrony} = \sigma_1 / \sum_{\ell=1}^M \sigma_{\ell} \quad (9)$$

Note that, as $\sum_{\ell=1}^M \sigma_{\ell} = 1$ due to the normalization of the window $\mathbf{F}_i(j)$ the synchrony can be simply estimated by σ_1 , $\sigma_1 \in [0, 1]$.

2.3. Data and preprocessing

Datasets: Human MRI datasets used in this study were sourced from the WU-Minn Human Connectome Project (HCP) database (Van Essen et al., 2013; Smith et al., 2013), which included a 128 subject sub-group (54% female, age range = 22–37) that passed image quality control criteria and completed all imaging acquisitions. The datasets comprised resting-state fMRI, motor-task fMRI, T1-weighted MRI and diffusion-weighted MRI (DWI) and were downloaded from the HCP repository as minimally preprocessed data. The HCP data acquisition was approved by the Washington University Institutional Review Board and informed consent was obtained from all subjects. Parameters of MRI acquisitions and the minimal preprocessing are fully described in reference (Glasser et al., 2013). The HCP motor task contained 16 blocks, each of which consisted of a visual cue (3 s) and ten identical movement trials (12 s). Five movement types were included in the task—right hand, left hand, right foot, left foot, and tongue, each of which was repeated once. The dataset was separated into two groups: the first 64 subjects for a primary dataset and other 64 subjects for an independent validation dataset.

Preprocessing: The HCP preprocessed functional and diffusion data are in different neurological spaces (fMRI data in ACPC space; and DWI data in MNI space). Reasonably accurate co-registration of images between the two MRI modalities, which typically involves nonlinear transformations, is critical for the proposed approach. In this work, the HCP preprocessed fMRI volumes were nonlinearly registered into ACPC space, and then up-sampled to the voxel resolution of the DWI data (i.e., 1.25 mm isotropic). This spatial transformation was performed by leveraging the `mni2acpc.nii` displacement maps provided within the HCP preprocessed data. Note that the ACPC space was chosen as the working space in this study to avoid a spatial transformation on DWI data that would necessitate a complex adjustment of axonal orientations (Alexander et al., 2001). In addition, the segmentation volumes (`aparc+aseg.nii`) provided within the HCP data were down-sampled to the working resolution, from which a WM mask was created. Further preprocessing of fMRI data in this study included four steps as follows. First, cerebrospinal fluid (CSF) nuisance signals and 12 variates of head motion were regressed out from time courses of fMRI data. Second, the volumes of fMRI data within the WM mask were spatially smoothed with a Gaussian smoothing kernel of 3-mm full width at half maximum. Spatial smoothing this way could prevent signal contamination from nearby GM. Note that, besides improving the signal-to-noise ratio in BOLD time courses, the spatial smoothing can reduce the sensitivity of the proposed approach to potential co-registration errors at some cost of spatial specificity. Third, time courses were bandpass filtered to retain frequencies from 0.01 to 0.10 Hz. Finally, the means of the filtered time courses were subtracted, and the data then

normalized to unit variance. In the HCP datasets, each session of fMRI (resting state/motor task) comprises two runs (left-to-right and right-to-left phase encoding). In this study, the two runs were temporally concatenated for each session to improve the performance of FAIW-PCA and counterbalance potential effects of the phase-encoding. Note that, for the motor task data, time frames of the two runs were truncated to be the same as those of the resting-state data before the concatenation.

2.4. Synchrony mapping using FAIW-PCA

Synchrony mapping using FAIW-PCA was performed on the HCP image data that had been co-registered in ACPC space. To begin with, a whole brain graph was constructed for each subject using the afore-mentioned approach with HARDI data. Following reference Abramian et al., 2021), two tuning parameters $\{\alpha, \beta\}$ were set to $\{0.9, 50\}$ in the generation of the graph so that the nature of elongated fibers can be characterized with high fidelities. With the graph constructed, the two-step activation mapping described in Sections II(2.1) and II(2.2) was performed voxel-wise: (1) a local fiber-architecture-informed window was created for each voxel by the spectral kernel approach, and (2) FAIW-PCA was performed to estimate the synchrony of fMRI time-courses on the basis of fiber architecture information within the window. The parameter of the kernel τ , which determines the spatial extent of signal diffusion on fibers, was optimized to ensure the distribution of the synchrony σ_1 ($\sigma_1 \in [0, 1]$) in WM was peaked around 0.5.

2.5. Validation of FAIW-PCA-based activation mapping

We validated the proposed approach at a group level in MNI space. To do so, synchrony maps computed from each subject in the primary dataset and the independent validation dataset were co-registered into MNI space by leveraging the `acpc2mni.nii` displacement maps provided within the HCP preprocessed data. Then, an additional co-registration is performed between synchrony maps estimated from resting state and motor task using SPM12. Finally, the individual synchrony maps averaged to yield group-average synchrony maps. Then, to characterize the task-induced changes in synchrony, difference maps were calculated as

$$\Delta syn = \frac{2 \times (S_M - S_R)}{S_M + S_R} \quad (10)$$

where S_R and S_M are the synchronies measured in resting state and motor task, respectively; values of Δsyn indicate the strength of neural responses to the task. The group-average synchrony maps and their difference maps estimated from the primary dataset were analyzed as follows: (1) the group-average synchrony maps from resting states were investigated first by reference to anatomical structures conveyed by T_1 -weighted ($T_1 w$) images and fractional anisotropy maps derived from the HARDI data. (1) fiber tracking was implemented in the DSI Studio software package Yeh et al., 2010) to extract WM regions related to the primary motor cortex (M1) and the auditory cortex (A1&A2); the synchrony maps from the two functional states were compared with an emphasis on the M1 related WM regions; the auditory cortex is mainly associated with processing auditory information, which is in principle not involved in motor tasks and expected to undergo

minimal variations between the two functional states; thus, the specificity of the proposed approach was assessed by comparing the increase in WM activations under the motor task in the task-related and unrelated regions. (3) the regional synchronies were compared between the two functional states using the HCP tractography atlas of WM available on the website: <http://brain.labsolver.org/diffusion-mri-templates/tractography>. (4) group level statistical maps of syn-based activation were compared with those of GLM-based activation; the GLM-based activation mapping was performed with the preprocessed task fMRI data that underwent identical spatial smoothing and regressions of nuisance signals including cerebrospinal fluid and head motion; the GLM based activation mapping was implemented using SPM12 (<https://www.fil.ion.ucl.ac.uk/spm/software/spm12>), where the task conditions were convolved with a canonical HRF to generate five predictors that were included in the motor model –right hand, left hand, right foot, left foot, and tongue; each predictor covered the duration of 10 movements trials (12 s); the 3 s cue period prior to each motor block was modeled separately to account for visual activation related to the cue word presented on the screen at the beginning of each block; linear contrasts were computed to estimate activation for each movement type versus baseline and versus all other movement type; on a single subject level, conditions were contrasted against each other to create a parametric image that reflected the percent signal changes invoked by the tasks; on the group level, a one sample *t*-test was applied to the parametric images across all subjects to create a map of the brain activation; finally, activated voxels were reported at a threshold $P < 0.05$ with family-wise error rate (FWE) correction. (5) comparisons of syn-based activation maps between the primary dataset and the independent validation dataset were performed to validate the reproducibility of the proposed approach.

3. Results

Fig. 2 shows group-average synchrony maps reconstructed with the motor-task fMRI dataset collected from 64 participants in HCP, and FA color maps reconstructed with the DTI dataset from a representative participant as well as T_1 w images. Many continuous structures can be observed with high synchrony in both GM and WM. In the GM, the synchronous structures agree grossly with anatomical structures identified in the T_1 w images. In the WM, synchronous structures exist almost exclusively in regions that contain large axonal fascicles, with some typical examples denoted by red arrows that exhibit uniform fiber orientations in the FA color maps. These spatial patterns in WM are reasonable in terms of their relationship to functional neuroanatomy. For instance, the fiber bundles in occipital WM convey mainly visual signals so that voxels within them tend to have synchronous BOLD signals. Conversely, the WM regions that include fibers with heterogenous orientations (indicated by heterogeneities in FA colors) or crossing fibers (visualized as dim FA colors) exhibit low values in the synchrony maps, which can be appreciated in the regions denoted by green arrows in Fig. 2. This is explainable by the fact that the fibers leading to different locations in GM tend to have asynchronous neural activities and thus asynchronous BOLD signals.

Fig. 3 compares the group-average synchrony maps estimated from the resting-state and motor-task fMRI data on the basis of WM tractograms, in which the motor-task-related brain activations can be visually appreciated. In Fig. 3A&B, M1 and A1&A2 related WM regions

were determined by using fiber tracking with seed points defined in the corresponding cortical regions. It can be seen that, in both M1 GM regions and the related WM regions, the synchrony maps exhibit substantially higher intensities during the motor task than in the resting-state. Coactivations of the associated GM and WM regions are quantitatively visualized by the maps of synchrony difference (Δsyn) between the two states in the bottom row of Fig. 3C. In contrast, the WM regions associated with the auditory cortex have no significant changes between the two states. The changes in synchrony in M1 and A1&A2 related WM regions are further compared in Fig. 4, in which the synchronies during the motor task are plotted against those from the resting state. The offset distances of points in the scatter plots from the identity line reflect changes in WM voxels. Here, the changes in BOLD signals in the M1-related region are substantially larger than those of the A1&A2 related WM region, in which the scatter points are tightly and symmetrically distributed along the identity line. Unexpectedly, no obvious increases in synchrony are observed in the internal capsule while some increases are observed in the WM regions that are not connected with M1. In addition, the difference maps exhibit a broad asymmetry, where the deep WM regions in the left hemisphere show more broad increased synchronies than the right counterpart of the brain.

Fig. 5 compares the synchronies of time courses collected from the resting state and motor task data. These time courses are extracted in a FAIW that associated with a typical voxel in the M1 related WM tract, where the typical voxel is determined in a Δsyn map estimated from a single subject by selecting a voxel with a high intensity. The paradigm of the HCP motor task in Fig. 5A provides a reference for the analysis of the time courses. In Fig. 5B and C, the 1st principal component (PC) of FAIW-PCA and color maps show overall temporal patterns of time courses from the two states. Note that the PCs derived from the two states exhibit no obvious dependences on the timing of the motor task. On the other hand, the synchrony of the time courses from the motor task shows an increase compared with those from the resting state, which is quantified by the first eigenvalue of FAIW-PCA (σ_1) and can be intuitively appreciated by comparing the color maps that show the coherence of the time courses across the voxels (i.e., along the vertical direction) in the corresponding FAIW. In summary, the analysis of time courses demonstrates the nonlinear nature of WM hemodynamics and the limitation of the GLM assumption in WM that implies a linear correspondence between the BOLD time courses and the external paradigm of the task, which demonstrates that the synchrony is a more robust metric for activation mapping without any model assumptions.

In Fig. 6, tract-wise changes in synchrony from resting state to motor task are examined for 46 fiber tracts defined in the HCP population-averaged tractography atlas. Fig. 6A shows statistical comparisons for each fiber tract, where paired student tests were used to identify significant changes in tract-averaged synchronies from 64 individual subjects. As seen, the synchrony during the motor task significantly increased for 34 fiber tracts with $P < 0.05$, and for 15 fiber tracts with $P < 0.01$. Among those tracts that changed, the majority are directly engaged in sensorimotor functions or visual processing including tracts in/linking the cerebellum and brainstem (cerebellum (CB), middle cerebellar peduncle (MCP), superior cerebellar peduncle (SCP), inferior cerebellar peduncle (ICP), vermis (V) and medial lemniscus (ML)) (Catani and Thiebaut de Schotten, 2008; Dell'Acqua et al.,

2013), the corticospinal tract (CST) (Cho et al., 2007), the corpus callosum (CC) (Saenz and Fine, 2010) and the optic radiation (OR) (Hofer et al., 2010). Note that many fiber tracts that are not directly involved in motor function or vision also show changes in Fig. 6A presumably because they are associated with motor network indirectly. For instance, the observed changes in the corticostriatal pathway (CS) may be explained by its role in motor planning as this fiber tract connects to the putamen, a main basal ganglia structure responsible for motor control (Haber, 2016). Tract-wise increases in synchrony are further visually illustrated in Fig. 6B. Here, the differences in tract-averaged synchrony are assigned as intensities to the corresponding tracts with significant increases in synchrony ($P < 0.05$), which are then displayed as 2D images using maximum intensity projection for axonal, sagittal and coronal views. High intensities in the figure appear mainly along the CST, consistent with the functional dominance of the sensorimotor pathways involved in the execution of the motor task.

Fig. 7 compares group level statistical maps of γ -syn-based and GLM-derived changes (B), with FA color maps as anatomical references of WM (A). In the statistically inferred activation maps from both approaches, t-values thresholded with FDR-corrected P values of 0.05 are shown in Fig. 7B. The GLM-indicated activation maps show that the whole M1 cortical region is engaged by the composite task that includes foot, hand and tongue movements, which agree well with previous results (Barch et al., 2013). Besides, the insular cortex that is engaged in motor control also exhibits activations in GLM statistical maps. The γ -syn-based results also highlight the cortical region of M1 with smaller coverages in the tongue motor cortex and insular cortex than the GLM-based activations. This can be actually deduced from Fig. 3 in which these regions in γ -syn-based activation maps have similarly high synchronies in both the resting state and the motor task. On the other hand, there are significant γ -syn-based changes in WM regions that are hardly captured by the GLM approach. These detected activations span large WM regions that are directly or indirectly associated with M1 (See the preceding paragraph). This demonstrates the power of our approach to detect functional changes in WM, though some of the detected changes in WM appear to be more disperse or discontinuous than in GM. This phenomenon may largely be attributable to inter-subject variabilities of functional structures in WM, which typically have elongated geometry, thus tending to confound group level statistical analyses due to imperfect registrations. These spatial variabilities are demonstrated by the synchrony structures denoted by the red arrows in Fig. 7C, which shows synchrony maps of three typical subjects that have been registered into MNI space. In spite of the use of fine nonlinear registrations, elongated subtle synchrony structures in WM show discernable spatial variations among these subjects.

Fig. 8 demonstrates the reproducibility of the FAIW-PCA activation mapping, which is validated by two independent datasets (Group 1 and Group 2). The group-average γ -syn maps estimated from the two datasets are displayed in Fig. 8A, which show very similar spatial patterns of the enhancement of synchrony by the task. Fig. 8B,C show statistical t maps of γ -syn-based activations for the two datasets, which are thresholded with FDR-corrected P values of 0.05. To quantify the similarity between the activation maps from the two datasets, the Dice coefficient was calculated as

$$D = \frac{2 | M_{G1} \cap M_{G2} |}{| M_{G1} | + | M_{G2} |} \quad (11)$$

where M_{G1} and M_{G2} are two sets of activated voxels detected from Group 1 and Group 2, respectively and $| \cdot |$ denotes set cardinality. The Dice coefficient is constrained to the range of $[0, 1]$ (Gawryluk et al., 2014), where a value 1 signifies perfect overlap between the two maps and a value 0 represents no overlap. In this study, Dice coefficients of the two activation maps in B is 0.76, which demonstrates a high reproducibility of the FAIW-PCA activation mapping.

4. Discussion

Localizing neural activations under specific functional loadings is fundamental to understanding the functional organization of the brain. GLM-based activation mapping has been the standard approach for detecting and localizing task-evoked activations in GM, and assumes that BOLD signals in response to neural activation can be modeled by convolving the time course of neural activity with a fixed HRF that is determined a priori (Boynton et al., 2012). However, this approach is inappropriate for WM. In this study, we proposed a model-free approach to detect changes in BOLD signals associated with neural activities in WM by measuring the enhancement of synchrony in WM BOLD signals during a functional task. The model-free approach draws upon an assumption that, under functional loadings, BOLD signals in relevant WM fibers are modulated by stimulus-evoked neural responses and thereby become more synchronized than in a resting state. This approach consists of two major steps. First, a fiber-architecture-informed spatial window is created with ODFs constructed from HARDI data, which characterizes a topographically defined neighborhood of a voxel that is isomorphic to local fiber architectures within WM. Second, a modified PCA is used to estimate the synchrony of BOLD signals based on the spatial window. The proposed approach is validated using a cohort of 3T fMRI datasets from the HCP, which demonstrates that the changes associated with neural activation can be reliably detected as enhancements of fMRI signal synchrony in the fibers that are engaged in the presented task.

Structures defined by intrinsic synchronous signals exist in both GM and WM and have similar boundaries with other definitions of anatomical and functional structures (Fig. 2). For GM, they appear as separable volumes with low degrees of anisotropy that are consistent with identifiable functional areas or units that to date have been implicitly assumed in the study of the functional connectome (i.e., Brodmann areas). In contrast to GM, functional units of WM measured by fMRI are elongated fibers that facilitate the transmission of neural signals along the fibers, which are identifiable by WM synchrony structures shown in Figs. 2 and 7C at group and individual levels, respectively. These synchrony structures can be clearly observed in a resting state and become more pronounced in functionally-relevant structures under task loading (Fig. 3), which agrees with previous findings that correlations of BOLD signals in relevant WM bundles increase with tasks (Ding et al., 2013; Ding et al., 2016; Schilling et al., 2019). Note that the regions that contain parallel fascicles tend to have higher levels of synchrony than those with incoherent orientations because some fibers in the latter scenario are in principle connected to different functional units in GM such

that the synchrony of BOLD signals is not apparent. Compared with synchrony structures that are merely derived from fMRI data (Zhao et al., 2022), the fiber-architecture synchrony structures characterize more spatial details in WM.

By comparing group-average synchrony maps derived from resting-state and motor-task fMRI data, we demonstrate that BOLD signal synchrony can be enhanced by task loading in both GM and WM (Fig. 3-6). For the GM, group level statistical maps of δ -syn-based activations in the M1 region show a moderate overlap with those of GLM-based activations, although with a smaller coverage than the latter, especially in the tongue motor cortex and the insular cortex (Fig. 7). The missing voxels of δ -syn-based activations in the tongue motor cortex may be explained by subconscious swallowing activity that inevitably occurs during the resting state acquisitions, which is implied by the observation in Fig. 3 that the missing regions in δ -syn-based activation maps have similar synchronies in both the resting state and the motor task. Likewise, the insular cortex, which possesses multiple functions such as interoceptive attention, multimodal sensory processing, autonomic control and perceptual self-awareness (Nieuwenhuys, 2012; Benarroch, 2019), may be equally activate in the two states, and thus show similar synchronies. The δ -syn maps exhibit large increases in the M1-related WM regions in Fig. 3, which demonstrates that δ -syn-based activation mapping possesses a distinctive capability to detect activity-related signal changes in WM that are not captured by the GLM approach. This highlights the possibility that changes in synchrony do not depend on net increases in BOLD signal. Further statistical analysis based on a population-averaged tractography atlas demonstrate that many fiber tracts that are indirectly associated with M1 also show significant enhancements of BOLD signal synchrony (Fig. 6). Although many WM regions are involved in the motor task (Gonzalez-Castillo et al., 2012), the M1-related WM exhibit most significant changes, as shown Fig. 6B. In addition, some WM regions that are not directly associated with the motor cortex also exhibit substantial enhancements of synchrony under the motor task (Fig. 3), which poses challenges in interpreting δ -syn maps. One potential explanation is a massive engagement of WM in the execution of the motor task, which is implied by earlier reports that GM across almost the entire brain can be activated by a simple task (Gonzalez-Castillo et al., 2012).

A high reproducibility of the proposed approach was demonstrated in this study, while its sensitivity and specificity warrant further studies. As shown in Fig.8, the reproducibility of the proposed approach was validated using two independent groups of participants where statistical t maps reports δ -syn-based activations thresholded with the FDR-corrected P values of 0.05. Dice coefficient of the activation maps estimated from the two groups is 0.76, which demonstrates high reproducibility of the FAIW-PCA activation mapping (Fig. 8). The δ -syn-based activations can be clearly observed in the M1-related WM regions that are closer to the cortical surface. However, no substantial increases in synchrony are observed in the internal capsule that includes the pathways of CST, which suggests a limited sensitivity of the proposed approach. There are two potential reasons for the unexpected phenomena. First, the targeted projection pathways pass through the anterior two-thirds of the posterior internal capsule, so that this portion contains densely packed fiber bundles each projecting to a different area of the motor cortex. In the HCP task paradigm used for this work, these fiber bundles are selectively activated but in a sequential manner, which could decrease the temporal synchrony in nearby voxels in this region. Second, the SNR in this deep WM

region is insufficient for a reliable detection because the sensitivity of the receiver coil is much lower than the regions that are closer to the cortical surface. In addition, the lower sensitivity of the receiver coil in deep WM regions along with the dextrorality of the subjects at a group level may account for the asymmetry observed in the difference map. Not to our expectations, there are substantial enhancements of synchrony in many WM regions that are not directly connected with the M1, which warrants a further validation of the specificity of the proposed approach. For example, the specificity can be more comprehensively investigated by comparing activation maps estimated from different tasks that activate distinct WM regions. Ideally, standard task designs with identical repeated tasks and relative longer rest periods will be more effective for the validation of the specificity than the HCP motor task design that involves a mixture of different motor tasks.

To validate the proposed approach with large-sample datasets, we analyzed the open-access HCP datasets of 128 participants, though the parameters of MRI acquisition and the designs of the fMRI tasks were not tailored for our study, which thus led to some limitations. First, parameters of MRI acquisitions in the HCP data are optimized for fMRI of GM. In a future study, the parameters of MRI acquisitions can be optimized for detecting synchrony of BOLD signals in WM, which may not require high temporal resolution. The short repetition time used in the HCP fMRI acquisition with a relatively high temporal resolution could lead to an insufficient signal recovery (i.e., T_1 relaxation) between successive volume acquisitions, in which the net magnetization in a voxel of 3D fMRI volume cannot ensure an SNR that allows for reliable measurements of BOD signals. On the other hand, a longer TR could result in more physiological contaminations in fMRI signals via cardiorespiratory aliasing (Raitamaa et al., 2019). Hence, a compromise between the two factors is necessary for a further optimization of temporal resolution. Note that the flip angle and the echo time along with the repetition time could be further synergistically optimized based on the relaxation times of WM. Second, the motor task of the HCP involves five different motions that produce only about 17 data points in each time course for each motion. Some regions in brain that are engaged by only one motion may be more difficult to be detected by our approach because the measurement of the synchrony is sensitive to the number of data points in time courses. This limitation in the task design can reduce the sensitivity of the proposed approach, which may be one reason for the loss of activations detected compared to the GLM results. In a future study, increasing the data points that are modulated by identical repeated stimuli can be used to increase the sensitivity of the proposed method, which may allow the FAIW-PCA-based activation mapping at a single-subject level.

5. Conclusions

The GLM-based activation mapping that is well-established for detecting BOLD signal changes in a task in GM is not well suited for studies of activity-related signal changes in WM. In this study, we proposed a model-free approach to detect task-evoked signal changes in WM by measuring increases in BOLD signal synchrony within local fiber architectures. Using the HCP datasets, we validated that the proposed approach could detect BOLD signal changes in WM fibers that engaged in the motor task with high sensitivities and reproducibility. This approach promises to provide a standardized tool to map neural responses in WM.

Acknowledgements

Data used in this work were provided by the Human Connectome Project, WU-Minn Consortium (Principal Investigators: David Van Essen and Kamil Ugurbil; 1U54MH091657) funded by the Institutes and Centers of the National Institutes of Health (NIH) that support the NIH Blueprint for Neuroscience Research; and by the McDonnell Center for Systems Neuroscience at Washington University. This work was supported by National Institutes of Health under Grant R01NS093669 and Grant R01NS113832.

Abbreviations:

GLM	General linear model
HRF	Hemodynamic response function
ODF	Orientation distribution functions
PCA	Principal component analysis
BOLD	Blood oxygenation level-dependent
WM	White matter
GM	Gray matter
HARDI	High angular resolution diffusion imaging

References

- Gawryluk JR, Mazerolle EL, D'Arcy RC, 2014. Does functional MRI detect activation in white matter? A review of emerging evidence, issues, and future directions. *Front. Neurosci* 8, 239. [PubMed: 25152709]
- Mazerolle EL, Ohlhauser L, Mayo CD, Sheriff A, Gawryluk JR, May 2020. Evidence of underreporting of white matter fMRI activation. *J. Magn. Reson. Imaging* 51 (5), 1596–1597. [PubMed: 31667922]
- Gore JC, Li M, Gao Y, Wu TL, Schilling KG, Huang Y, Mishra A, Newton AT, Rogers BP, Chen LM, Anderson AW, Ding Z, 2019. Functional MRI and resting state connectivity in white matter - a mini-review. *Magn. Reson. Imaging* 63 (Nov), 1–11. [PubMed: 31376477]
- Grajauskas LA, Frizzell T, Song X, D'Arcy RCN, 2019. White matter fMRI activation cannot be treated as a nuisance regressor: overcoming a historical blind spot. *Front. Neurosci* 13, 1024. [PubMed: 31636527]
- Lin TH, Spees WM, Chiang CW, Trinkaus K, Cross AH, Song SK, 2014. Diffusion fMRI detects white-matter dysfunction in mice with acute optic neuritis. *Neurobiol. Dis* 67 (Jul), 1–8. [PubMed: 24632420]
- Spees WM, Lin TH, Song SK, 2013. White-matter diffusion fMRI of mouse optic nerve. *Neuroimage* 65, 209–215 Jan 15. [PubMed: 23085108]
- Spees WM, Lin TH, Sun P, Song C, George A, Gary SE, Yang HC, Song SK, Oct 23, 2018. MRI-based assessment of function and dysfunction in myelinated axons. *Proc. Natl. Acad. Sci. USA* 115 (43), E10225–E10234. [PubMed: 30297414]
- Olszowy W, Diao Y, Jelescu IO, 2021. Beyond BOLD: evidence for diffusion fMRI contrast in the human brain distinct from neurovascular response. *bioRxiv*.
- Ding Z, Huang Y, Bailey SK, Gao Y, Cutting LE, Rogers BP, Newton AT, Gore JC, 2018. Detection of synchronous brain activity in white matter tracts at rest and under functional loading. *Proc. Natl. Acad. Sci. USA* 115 (3), 595–600 Jan 16. [PubMed: 29282320]

- Gao Y, Li M, Huang AS, Anderson AW, Ding Z, Heckers SH, Woodward ND, Gore JC, 2021. Lower functional connectivity of white matter during rest and working memory tasks is associated with cognitive impairments in schizophrenia. *Schizophr. Res* 233, 101–110 Jul. [PubMed: 34215467]
- Jiang Y, Luo C, Li X, Li Y, Yang H, Li J, Chang X, Li H, Yang H, Wang J, Duan M, Yao D, 2019. White-matter functional networks changes in patients with schizophrenia. *Neuroimage* 190, 172–181 Apr 15. [PubMed: 29660513]
- Huang Y, Bailey SK, Wang P, Cutting LE, Gore JC, Ding Z, 2018. Voxel-wise detection of functional networks in white matter. *Neuroimage* 183, 544–552 Dec. [PubMed: 30144573]
- Marussich L, Lu KH, Wen H, Liu Z, 2017. Mapping white-matter functional organization at rest and during naturalistic visual perception. *Neuroimage* 146, 1128–1141 Feb 1. [PubMed: 27720819]
- Ji GJ, Ren C, Li Y, Sun J, Liu T, Gao Y, Xue D, Shen L, Cheng W, Zhu C, Tian Y, Hu P, Chen X, Wang K, 2019. Regional and network properties of white matter function in Parkinson's disease. *Hum. Brain Mapp* 40 (4), 1253–1263 Mar. [PubMed: 30414340]
- Li M, Gao Y, Ding Z, Gore JC, 2021. Power spectra reveal distinct BOLD resting-state time courses in white matter. *Proc. Natl. Acad. Sci* 118 (44).
- Li M, Newton AT, Anderson AW, Ding Z, Gore JC, 2019. Characterization of the hemodynamic response function in white matter tracts for event-related fMRI. *Nat. Commun* 10 (1), 1140 Mar 8. [PubMed: 30850610]
- Poline JB, Brett M, 2012. The general linear model and fMRI: does love last forever? *Neuroimage* 62 (2), 871–880 Aug 15. [PubMed: 22343127]
- Zhang D, Raichle ME, 2010. Disease and the brain's dark energy. *Nat. Rev. Neurol* 6 (1), 15–28 Jan. [PubMed: 20057496]
- Laird AR, Fox PM, Eickhoff SB, Turner JA, Ray KL, McKay DR, Glahn DC, Beckmann CF, Smith SM, Fox PT, 2011. Behavioral interpretations of intrinsic connectivity networks. *J. Cogn. Neurosci* 23 (12), 4022–4037 Dec. [PubMed: 21671731]
- Schilling KG, Janve V, Gao Y, Stepniewska I, Landman BA, Anderson AW, 2018. Histological validation of diffusion MRI fiber orientation distributions and dispersion. *Neuroimage* 165, 200–221 Jan 15. [PubMed: 29074279]
- Voigt FF, Kirschenbaum D, Platonova E, Pages S, Campbell RAA, Kastli R, Schaettin M, Egolf L, van der Bourg A, Bethge P, Haenraets K, Frezel N, Topilko T, Perin P, Hillier D, Hildebrand S, Schueth A, Roebroek A, Roska B, Stoeckli ET, Pizzala R, Renier N, Zeilhofer HU, Karayannis T, Ziegler U, Batti L, Holtmaat A, Luscher C, Aguzzi A, Helmchen F, 2019. The mesoSPIM initiative: open-source light-sheet microscopes for imaging cleared tissue. *Nat. Methods* 16 (11), 1105–1108 Nov. [PubMed: 31527839]
- Courtemanche MJ, Sparrey CJ, Song X, MacKay A, D'Arcy RCN, 2018. Detecting white matter activity using conventional 3 Tesla fMRI: an evaluation of standard field strength and hemodynamic response function. *Neuroimage* 169, 145–150 Apr 1. [PubMed: 29229580]
- Kay KN, David SV, Prenger RJ, Hansen KA, Gallant JL, 2008. Modeling low-frequency fluctuation and hemodynamic response timecourse in event-related fMRI. *Hum. Brain Mapp* 29 (2), 142–156 Feb. [PubMed: 17394212]
- Vincent T, Risser L, Ciuciu P, 2010. Spatially adaptive mixture modeling for analysis of FMRI time series. *IEEE Trans. Med. Imaging* 29 (4), 1059–1074 Apr. [PubMed: 20350840]
- Polimeni JR, Lewis LD, 2021. Imaging faster neural dynamics with fast fMRI: a need for updated models of the hemodynamic response. *Prog. Neurobiol* 207, 102174 Dec. [PubMed: 34525404]
- Yarkoni T, Barch DM, Gray JR, Conturo TE, Braver TS, 2009. BOLD correlates of trial-by-trial reaction time variability in gray and white matter: a multi-study fMRI analysis. *PLoS One* 4 (1), e4257. [PubMed: 19165335]
- Jochimsen TH, Ivanov D, Ott DV, Heinke W, Turner R, Moller HE, Reichenbach JR, 2010. Whole-brain mapping of venous vessel size in humans using the hypercapnia-induced BOLD effect. *Neuroimage* 51 (2), 765–774 Jun. [PubMed: 20188189]
- Zang Y, Jiang T, Lu Y, He Y, Tian L, 2004. Regional homogeneity approach to fMRI data analysis. *Neuroimage* 22 (1), 394–400 May. [PubMed: 15110032]

- Yuan R, Di X, Kim EH, Barik S, Rypma B, Biswal BB, 2013. Regional homogeneity of resting-state fMRI contributes to both neurovascular and task activation variations. *Magn. Reson. Imaging* 31 (9), 1492–1500 Nov. [PubMed: 23969197]
- Lv Y, Margulies DS, Villringer A, Zang YF, 2013. Effects of finger tapping frequency on regional homogeneity of sensorimotor cortex. *PLoS One* 8 (5), e64115. [PubMed: 23696867]
- Ding Z, Newton AT, Xu R, Anderson AW, Morgan VL, Gore JC, 2013. Spatio-temporal correlation tensors reveal functional structure in human brain. *PLoS One* 8 (12), e82107. [PubMed: 24339997]
- Ding Z, Xu R, Bailey SK, Wu TL, Morgan VL, Cutting LE, Anderson AW, Gore JC, 2016. Visualizing functional pathways in the human brain using correlation tensors and magnetic resonance imaging. *Magn. Reson. Imaging* 34 (1), 8–17 Jan. [PubMed: 26477562]
- Schilling KG, Gao Y, Li M, Wu TL, Blaber J, Landman BA, Anderson AW, Ding Z, Gore JC, 2019. Functional tractography of white matter by high angular resolution functional-correlation imaging (HARFI). *Magn. Reson. Med* 81 (3), 2011–2024 Mar. [PubMed: 30277272]
- Abramian D, Larsson M, Eklund A, Aganj I, Westin CF, Behjat H, 2021. Diffusion-informed spatial smoothing of fMRI data in white matter using spectral graph filters. *Neuroimage* 237, 118095 Aug 15. [PubMed: 34000402]
- Shuman DI, Narang SK, Frossard P, Ortega A, Vandergheynst P, 2013. The emerging field of signal processing on graphs: extending high-dimensional data analysis to networks and other irregular domains. *IEEE Signal Process Mag.* 30 (3), 83–98.
- Ortega A, Frossard P, Kovacevic J, Moura JMF, Vandergheynst P, 2018. Graph signal processing: overview, challenges, and applications. *Proc. IEEE* 106 (5), 808–828.
- Iturria-Medina Y, Canales-Rodriguez EJ, Melie-Garcia L, Valdes-Hernandez PA, Martinez-Montes E, Aleman-Gomez Y, Sanchez-Bornot JM, 2007. Characterizing brain anatomical connections using diffusion weighted MRI and graph theory. *Neuroimage* 36 (3), 645–660 Jul 1. [PubMed: 17466539]
- Turner R, 2002. How much cortex can a vein drain? Downstream dilution of activation-related cerebral blood oxygenation changes. *Neuroimage* 16 (4), 1062–1067 Aug. [PubMed: 12202093]
- Tian Y, Margulies DS, Breakspear M, Zalesky A, 2020. Topographic organization of the human subcortex unveiled with functional connectivity gradients. *Nat. Neurosci* 23 (11), 1421–1432 Nov. [PubMed: 32989295]
- Van Essen DC, Smith SM, Barch DM, Behrens TE, Yacoub E, Ugurbil K, Consortium, W.U.-M.H., 2013. The WU-Minn Human Connectome Project: an overview. *Neuroimage* 80, 62–79 Oct 15. [PubMed: 23684880]
- Smith SM, Beckmann CF, Andersson J, Auerbach EJ, Bijsterbosch J, Douaud G, Duff E, Feinberg DA, Griffanti L, Harms MP, Kelly M, Laumann T, Miller KL, Moeller S, Petersen S, Power J, Salimi-Khorshidi G, Snyder AZ, Vu AT, Woolrich MW, Xu J, Yacoub E, Ugurbil K, Van Essen DC, Glasser MF, Consortium, W.U.-M.H., 2013. Resting-state fMRI in the Human Connectome Project. *Neuroimage* 80, 144–168 Oct 15. [PubMed: 23702415]
- Glasser MF, Sotiropoulos SN, Wilson JA, Coalson TS, Fischl B, Andersson JL, Xu J, Jbabdi S, Webster M, Polimeni JR, Van Essen DC, Jenkinson M, Consortium, W.U.-M.H., 2013. The minimal preprocessing pipelines for the Human Connectome Project. *Neuroimage* 80, 105–124 Oct 15. [PubMed: 23668970]
- Alexander DC, Pierpaoli C, Basser PJ, Gee JC, 2001. Spatial transformations of diffusion tensor magnetic resonance images. *IEEE Trans. Med. Imaging* 20 (11), 1131–1139 Nov. [PubMed: 11700739]
- Yeh FC, Wedeen VJ, Tseng WY, 2010. Generalized q-sampling imaging. *IEEE Trans. Med. Imaging* 29 (9), 1626–1635 Sep. [PubMed: 20304721]
- Catani M, Thiebaut de Schotten M, 2008. A diffusion tensor imaging tractography atlas for virtual in vivo dissections. *Cortex* 44 (8), 1105–1132 Sep. [PubMed: 18619589]
- Dell'Acqua F, Bodi I, Slater D, Catani M, Modo M, 2013. MR diffusion histology and micro-tractography reveal mesoscale features of the human cerebellum. *Cerebellum* 12 (6), 923–931 Dec. [PubMed: 23907655]

- Cho SH, Kim DG, Kim DS, Kim YH, Lee CH, Jang SH, 2007. Motor outcome according to the integrity of the corticospinal tract determined by diffusion tensor tractography in the early stage of corona radiata infarct. *Neurosci. Lett* 426 (2), 123–127 Oct 16. [PubMed: 17897782]
- Saenz M, Fine I, 2010. Topographic organization of V1 projections through the corpus callosum in humans. *Neuroimage* 52 (4), 1224–1229 Oct 1. [PubMed: 20553894]
- Hofer S, Karaus A, Frahm J, 2010. Reconstruction and dissection of the entire human visual pathway using diffusion tensor MRI. *Front. Neuroanat* 4, 15. [PubMed: 20428499]
- Haber SN, 2016. Corticostriatal circuitry. *Dialogues Clin. Neurosci* 18 (1), 7–21 Mar. [PubMed: 27069376]
- Barch DM, Burgess GC, Harms MP, Petersen SE, Schlaggar BL, Corbetta M, Glasser MF, Curtiss S, Dixit S, Feldt C, Nolan D, Bryant E, Hartley T, Footer O, Bjork JM, Poldrack R, Smith S, Johansen-Berg H, Snyder AZ, Van Essen DC, Consortium, W.U.-M.H., 2013. Function in the human connectome: task-fMRI and individual differences in behavior. *Neuroimage* 80, 169–189 Oct 15. [PubMed: 23684877]
- Boynton GM, Engel SA, Heeger DJ, 2012. Linear systems analysis of the fMRI signal. *Neuroimage* 62 (2), 975–984 Aug 15. [PubMed: 22289807]
- Zhao Y, Gao Y, Li M, Anderson AW, Ding Z, Gore JC, 2022. Functional parcellation of human brain using localized topo-connectivity mapping. *IEEE Trans. Med. Imaging* Apr 20.
- Nieuwenhuys R, 2012. The insular cortex: a review. *Prog. Brain Res* 195, 123–163. [PubMed: 22230626]
- Benarroch EE, 2019. Insular cortex: functional complexity and clinical correlations. *Neurology* 93 (21), 932–938 Nov 19. [PubMed: 31645470]
- Gonzalez-Castillo J, Saad ZS, Handwerker DA, Inati SJ, Brenowitz N, Bandettini PA, 2012. Whole-brain, time-locked activation with simple tasks revealed using massive averaging and model-free analysis. *Proc. Natl. Acad. Sci. USA* 109 (14), 5487–5492 Apr 3. [PubMed: 22431587]
- Raitamaa L, Korhonen V, Huotari N, Raatikainen V, Hautaniemi T, Kananen J, Rasila A, Helakari H, Zienkiewicz A, Myllyla T, Borchardt V, Kiviniemi V, 2019. Breath hold effect on cardiovascular brain pulsations - A multimodal magnetic resonance encephalography study. *J. Cereb. Blood Flow Metab* 39 (12), 2471–2485 Dec. [PubMed: 30204040]

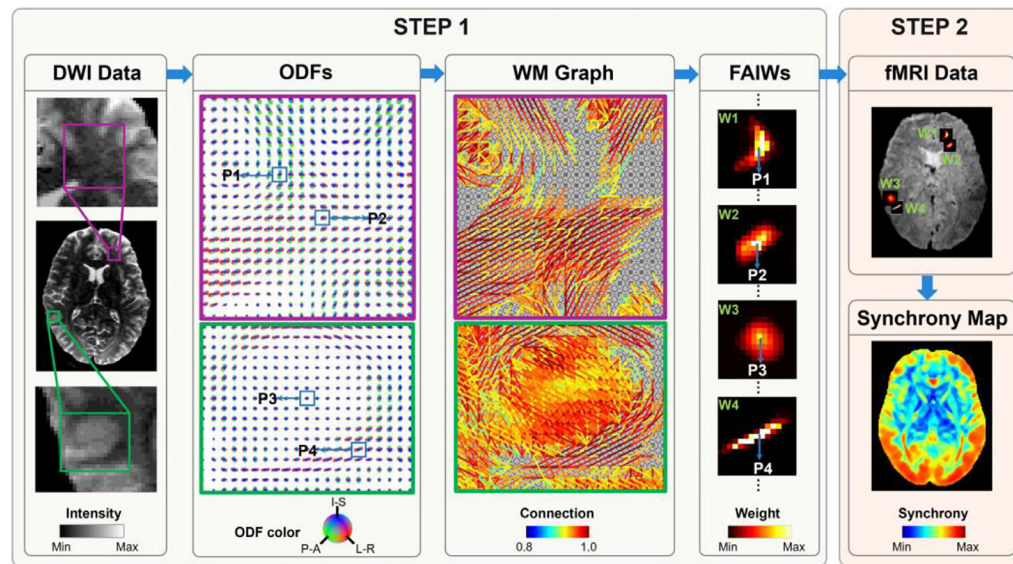


Fig. 1. Schematic of fiber architecture informed synchrony mapping in human white matter (WM). The algorithm of the proposed approach consists of two major steps. First, a spatial window is created for each voxel based on local fiber architectures. In this step, orientation distribution functions (ODFs) constructed from diffusion MRI data provide the information on fiber architectures, which are then used to generate a topological graph for WM. In this graph, every vertex corresponds to a voxel in MR images, with weighted connections to its neighbors. The edge weights are determined by the coherence between the directions of diffusion and the orientation of the graph edges. Then, diffusion on the graph with a point source located at each vertex is simulated to produce a diffusion profile that can be further used as a fiber-architecture-informed window (FAIWs). Here, typical FAIWs created for four voxels (**P1**, **P2**, **P3** and **P4**) demonstrate that they are adaptive to local fiber architectures. Second, a modified PCA is implemented to estimate the synchrony of fMRI time courses based on the FAIWs from the first step to yield activation maps. In the modified PCA, the FAIWs emphasize the time courses associated to voxels near the central position with high weights, which ensures the spatial specificity of the synchrony estimate.

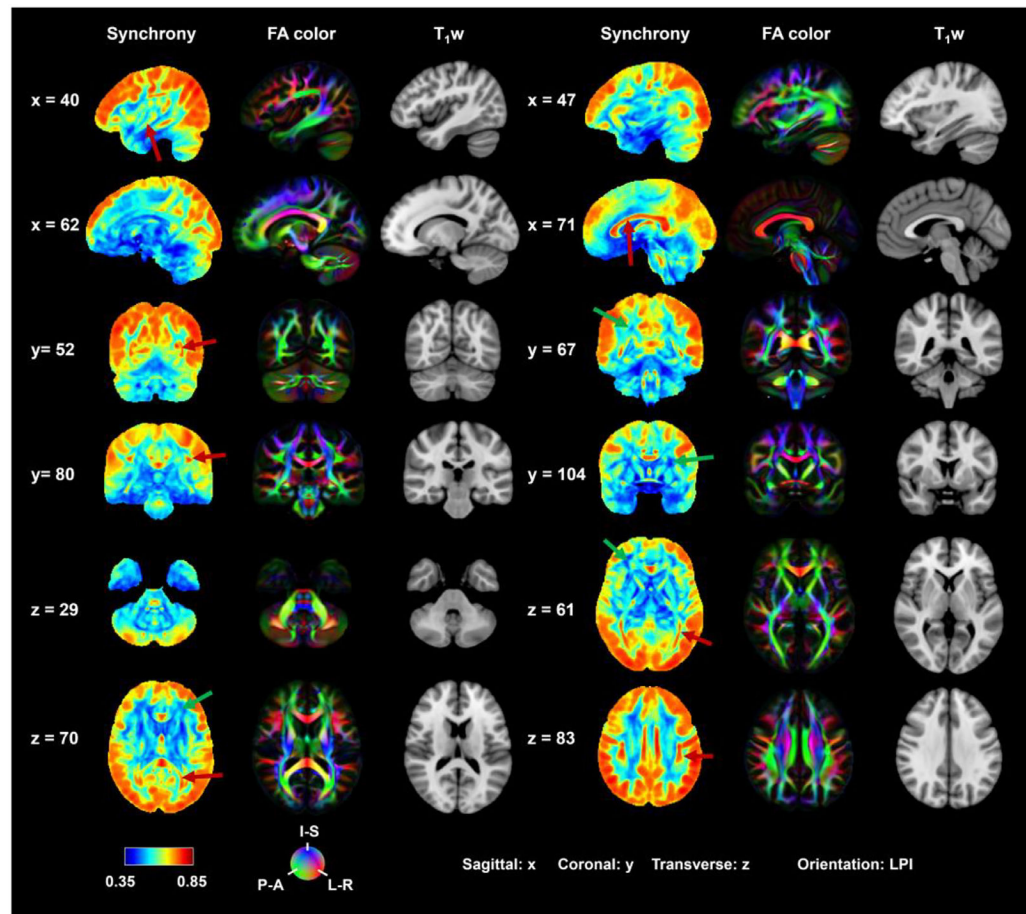


Fig. 2.

Group-average synchrony maps reconstructed with the motor-task fMRI dataset collected from 64 participants in HCP, and FA color maps reconstructed with the DTI dataset as well as T_1w images from a representative participant. There are many structures with high synchrony in both GM and WM. In the GM, the synchrony structures agree grossly with anatomical structures identified in the T_1w images. In the WM, synchrony structures exist almost exclusively in regions that contain large axonal fascicles, with some typical examples denoted by red arrows that exhibit uniform fiber orientations in the FA maps. Conversely, the WM regions that include fibers with heterogenous orientations (indicated by heterogeneities in FA colors) or crossing fibers (visualized as dim FA colors) exhibit low intensities in the synchrony maps, which is showcased in the regions denoted by green arrows.

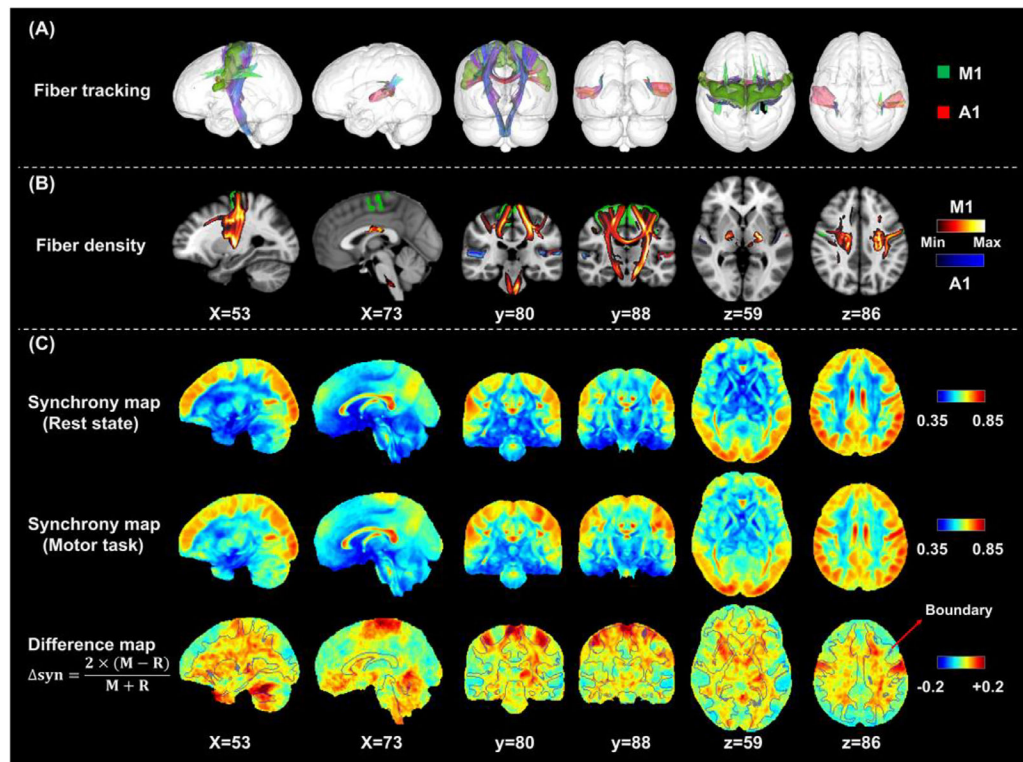


Fig. 3.

Comparison of group-average activation maps obtained from resting-state fMRI data and motor-task fMRI data on the basis of WM fiber tractograms. (A), exhibition of fiber tracking. The primary motor cortex (M1) and auditory cortex (A1&A2) related WM regions were determined by using fiber tracking with seed points defined in the corresponding cortical regions. (B), typical slices of fiber intensity maps estimated from fiber tracking. The fiber intensity of the M1 and A1&A2 related WM regions are displayed with red-yellow and blue colors, respectively. (C) synchrony maps and the corresponding difference maps displayed at the same slice indexes with the images in B. In both M1 GM regions and the related WM regions, the synchrony maps exhibit substantially higher intensities under motor task than those estimated from the resting-state, which demonstrates coactivations of the associated GM and WM regions. Note that dark lines are added in the difference maps to indicate the boundaries between the GM and WM.

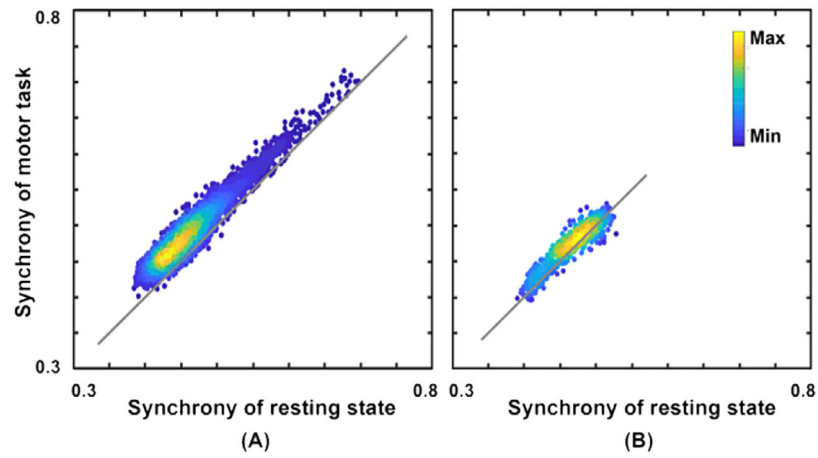
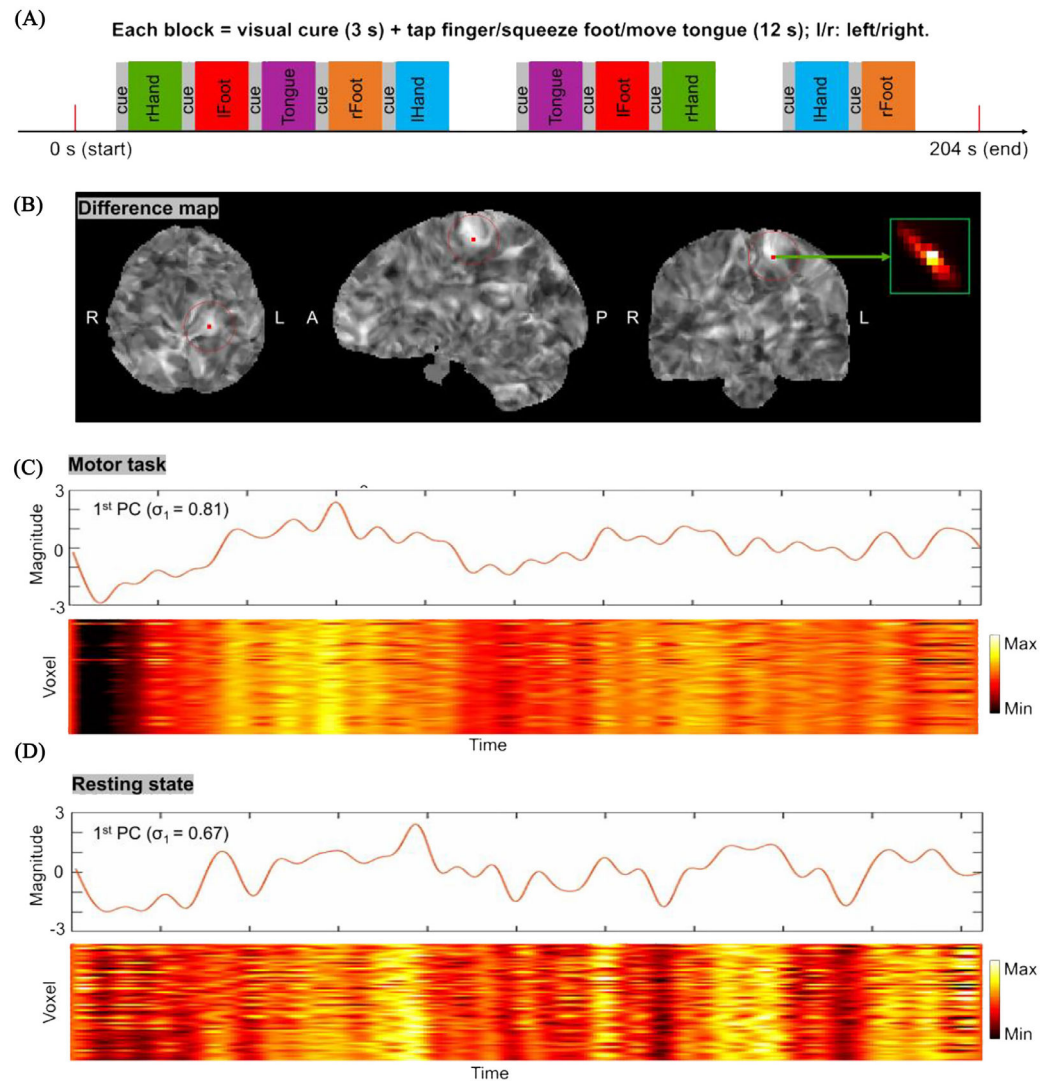


Fig. 4. Scatter plots of activations for the voxels in the primary motor-cortex (M1) related WM region (A) and the auditory cortex (A1&A2) related WM region (B). Distances from points to an identity line measure the degree of activations. Activations in the M1 related WM region are substantially higher than those of the A1&A2 related WM region, in which the scatter points are tightly and symmetrically distributed along the identity line.

**Fig. 5.**

Comparison of the synchronies of time courses collected from the resting state and motor task data at an individual level. (A), paradigm of the HCP motor task. The motor task contains 16 blocks, each of which consists of a visual cue (3 s) and ten identical movement trials (12 s). Five movement types are included in the task—right hand, left hand, right foot, left foot, and tongue, each of which is repeated once. The task paradigm provides a reference for the analysis of the time courses. (B), a typical syn map estimated from a single subject. Based on the syn map, the time courses are extracted from a FAIW of a typical voxel, which is determined in this map by selecting a voxel with a high intensity in the M1 related WM tract. (C&D), the 1st principal component (PC) of FAIW-PCA and color mapping of time courses from the resting state and motor task. They show overall temporal patterns of time courses. Note that the PCs derived from the two states exhibit no obvious dependences on the timing of the motor task. On the other hand, the synchrony of the time courses from the motor task shows an increase compared with those from the resting state, which is quantified by the first eigenvalue of FAIW-PCA (σ_1) and can be intuitively appreciated in the color

maps that show the coherence of time courses across the voxels (i.e., along the vertical direction) in the corresponding FAIW.

Author Manuscript

Author Manuscript

Author Manuscript

Author Manuscript

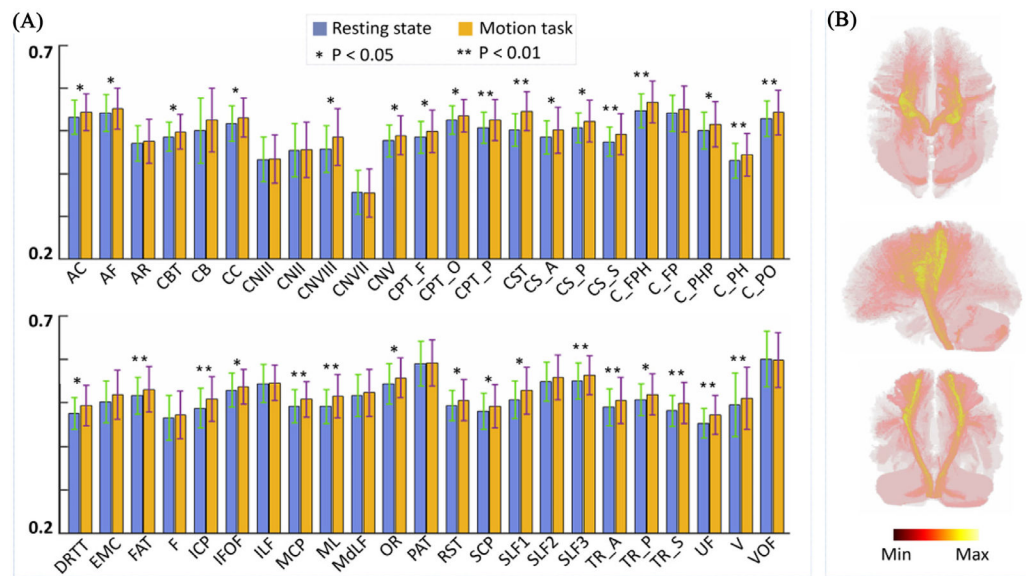


Fig. 6. Tract-wise comparison of synchrony between resting state and motor task for 46 fiber tracts defined in the HCP population-averaged tractography atlas. (A), statistical comparisons of synchrony for each fiber tract. Paired *t*-test was implemented with tract-averaged synchronies estimated individually from 64 subjects. The error bars indicate standard deviations of the tract-average synchronies across subjects. The result of statistical analysis shows that the synchrony under the motor task significantly increases for 34 fiber tracts with $P < 0.05$, and for 15 fiber tracts with $P < 0.01$. (B), maximum intensity projection images of differences in tract-averaged synchronies. To visually illustrate activations of the fiber tracts, the differences in tract-averaged synchrony are assigned as intensities to the corresponding tracts with significant increases in synchrony ($P < 0.05$), which are displayed as 2D images using maximum intensity projections for axonal, sagittal and coronal views. High intensities in the figure appear mainly along the CST, consistent with the functional dominance of the sensorimotor pathways involved in the execution of the motor task.

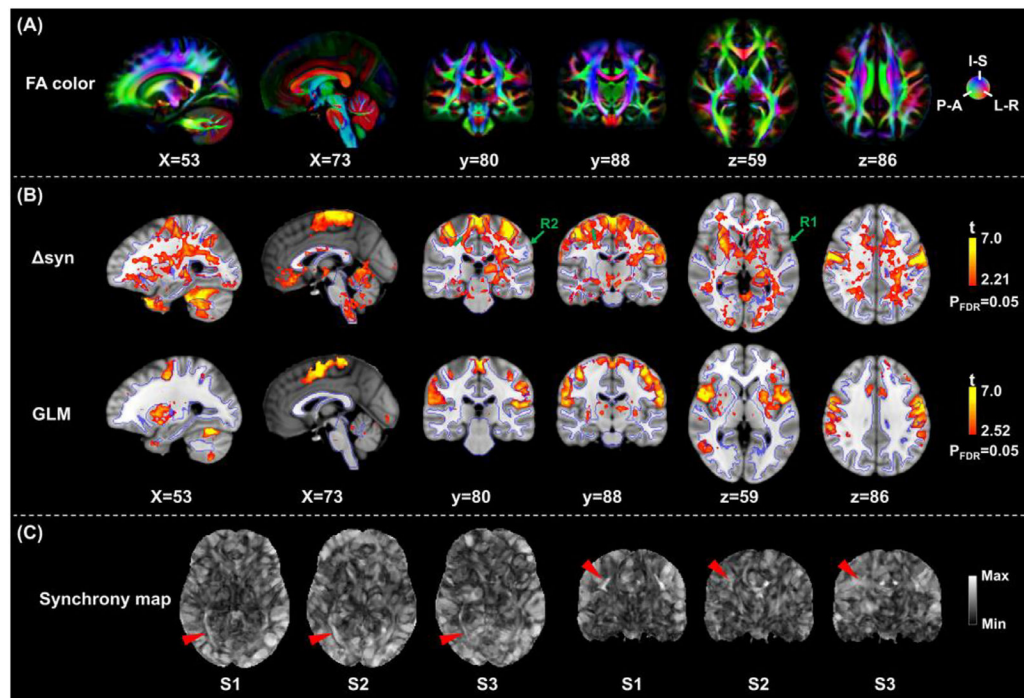


Fig. 7.

Comparison of group level statistical maps of Δ syn- and GLM-based activation with anatomical references of fiber structures. (A), FA color maps from one representative participant. The FA color maps show fiber structures. (B), group level statistical maps of Δ syn- and GLM-based activation. The statistical maps of Δ syn-based changes are derived by voxel-wise paired t-test of differences between resting state and motor task with a false discovery rate (FDR) correction for the 64-subject dataset. The statistical maps of GLM-based activation are estimated by using the standard SPM toolbox. In the statistically inferred activation maps from both the approaches, t-values thresholded with the FDR-corrected P values of 0.05 are shown in B. The GLM-based activation maps indicate that the whole primary motor cortex (M1) is engaged by the composite task that includes foot, hand and tongue movements. The Δ syn-based activations also highlight the cortical region of M1 and show smaller coverages in the insular cortex (R1) and the tongue motor cortex (R2) than the GLM-indicated activations. Moreover, the Δ syn-based activations exhibit in WM regions that are hardly captured by the GLM approach. The green arrows indicate the activations in WM that have similar spatial patterns with fiber structures identified in FA color maps. (C), synchrony maps of three typical subjects displayed in MNI space. There are discernable inter-subject variabilities of elongated fibers (indicated by red arrows) among these subjects, which could confound the statistical analysis at group level, and thus may account for the dispersity and discontinuity of activations detected in WM.

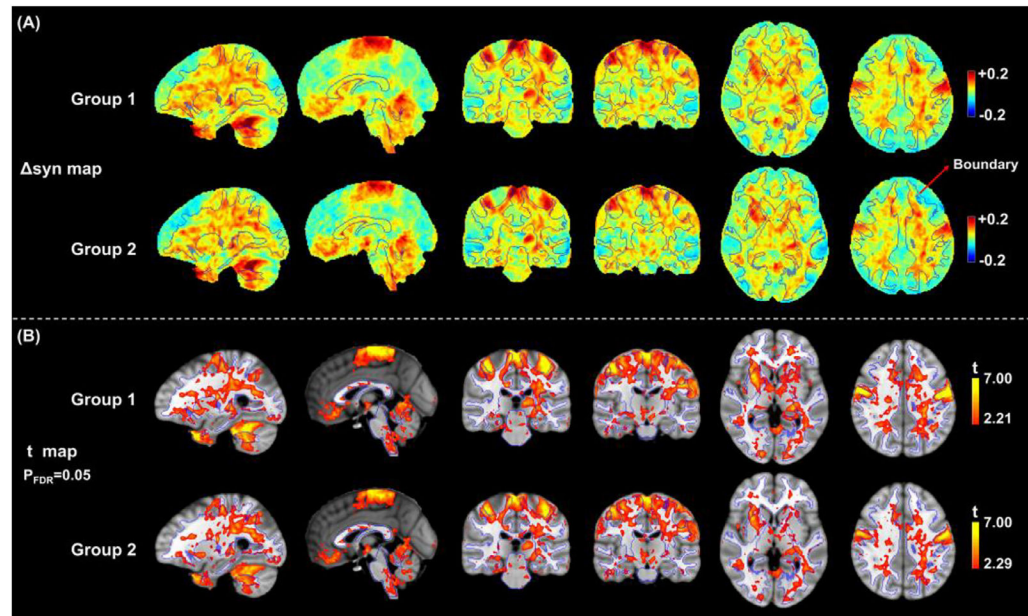


Fig. 8.

The reproducibility of the FAIW-PCA activation mapping validated with two independent datasets (Group 1 and Group 2). (A), group-average Δ syn maps estimated from the two datasets. The two maps exhibit similar spatial patterns of the task-induced enhancement of synchrony. (B), statistical t maps of Δ syn-based activation from the two datasets. In B, t values are thresholded with the FDR-corrected P values of 0.05. Dice coefficient is calculated to quantify the similarity between the activation maps from the two datasets. Dice coefficients of the two activation maps is 0.76, which demonstrates a good reproducibility of the proposed approach.